Dual-Doppler Observation of a Tornadic Storm

PETER S. RAY, R. J. DOVIAK, G. B. WALKER, D. SIRMANS, J. CARTER AND B. BUMGARNER

National Severe Storms Laboratory, NOAA, Norman, Okla. 73069

(Manuscript received 13 January 1975, in revised form 1 August 1975)

ABSTRACT

On 20 April 1974 a tornadic storm passed between the two NSSL Doppler radars spaced about 42 km apart. Both radars simultaneously collected Doppler data throughout the storm. Air motions synthesized from these data provide the first three-dimensional display of Doppler-derived wind fields in a tornadic storm. Cyclonic circulation, associated with the tornado, and regions of intense up- and down-drafts are clearly evident.

1. Introduction

The use of radar to infer dynamical structure from storms is extended by employing two or more coherent radars, positioned to allow construction of a three-dimensional wind field. A dual-Doppler technique to derive quasi-horizontal fields was first illustrated by Lhermitte (1970) and later extended by Frisch *et al.* (1974) to display all three Cartesian wind components within a Colorado snowstorm.

A tornadic storm passed between NSSL's two 10 cm Doppler radars spaced 42 km apart. This paper presents the first three-dimensional wind field analysis (i) within a tornadic storm (ii) based on 10 cm dual-Doppler observations (iii) assuming an anelastic fluid.

A low pressure center of about 996 mb was in eastern Colorado on 20 April 1974. A cold front extended through western Oklahoma and moved eastward about 25 km h^{-1} as the low pressure center moved NNE during the day. Surface dew points across Oklahoma were in the 50's but drier air was moving into the state from the southwest at 700 mb. Thunderstorms developed in central Oklahoma in the morning and moved NE about 17 m s^{-1}. During late morning a line of thunderstorms developed in western Oklahoma and intensified as they moved eastward.

The sounding presented in Fig. 1 was taken about 40 km north of Norman, starting at 1445 (all times CST) and ending about 40 min later. It revealed a conditionally unstable atmosphere with a deep moist layer near the surface, a profile favorable for convection. The moist layer at about 6 km is probably due to blow-off from an approaching storm, the storm which is the subject of this paper. The inversion at 7 km is probably due to descending air ahead of this storm. The decrease in ascent rate of the balloon at 4 km

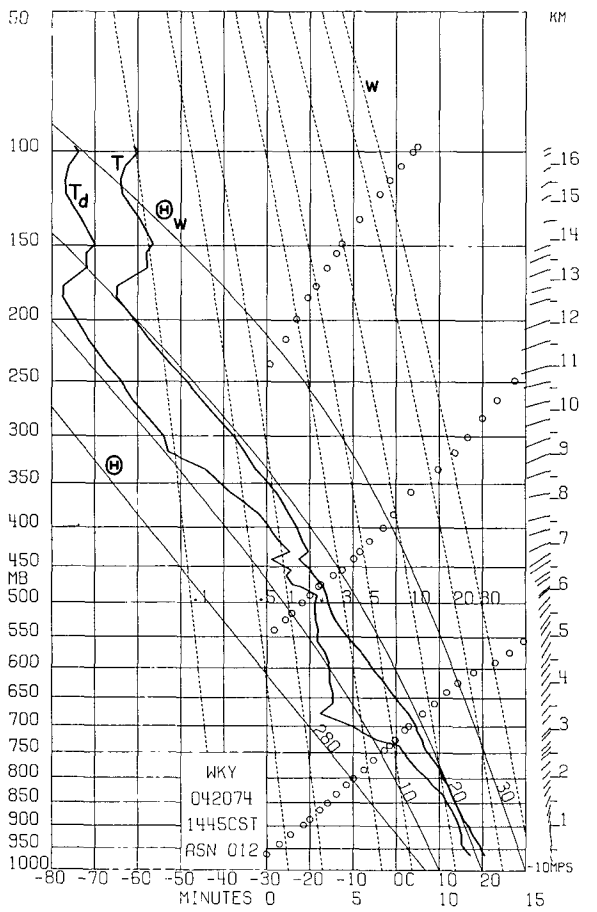

FIG. 1. Stüve diagram of sounding taken ahead of storm 1.5 h before data collection. Circles represent balloon ascent rate. Wind direction and magnitude are indicated on the right, with north being vertical and a 10 m s^{-1} magnitude scale is shown in the lower right corner.

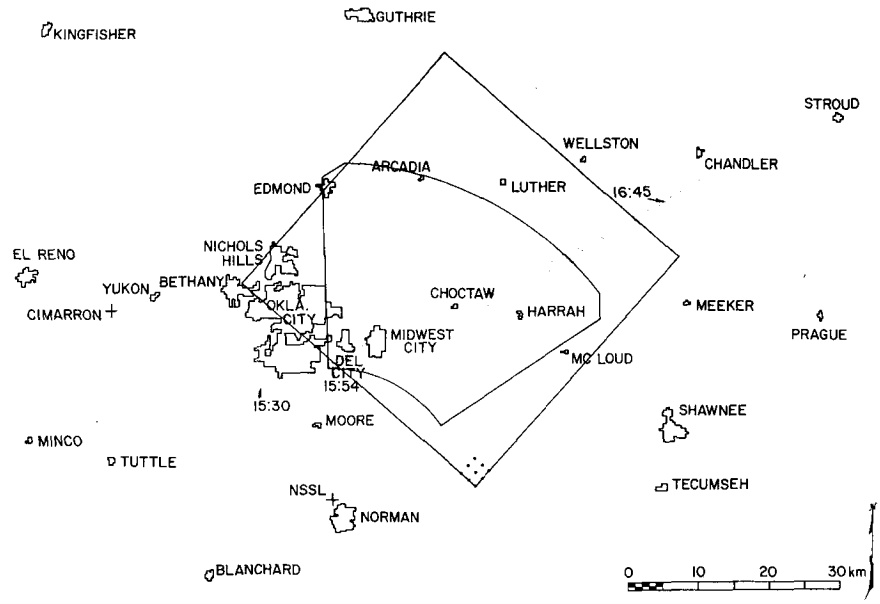

FIG. 2. Map of central Oklahoma showing the location of the two Doppler radars (Cimarron and Norman), the area of common Doppler coverage at 0° elevation, the area of analysis, the grid-point spacing (1.5 km), and the area encompassing tornado damage.

nearly coincides with the freezing level and is probably due to icing of the balloon.

A storm possessing hook echo signatures passed between the two NSSL Doppler radars about 1530. The data used in this paper were acquired about 1 h later, when the storm was approximately 40 km northeast of Norman and 60 km east of Cimarron.

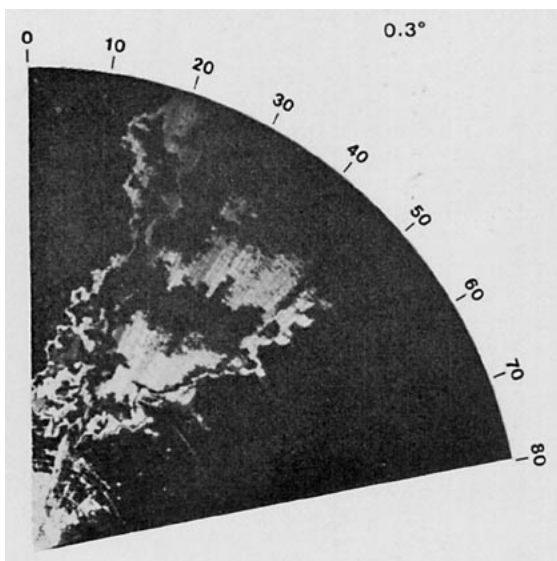

FIG. 3. Received power at Norman radar for an elevation angle of 0.3°. Regions of constant brightness correspond to the following categories of signal power in order of weakest to strongest signal: dim (−92 to −83 dBm), bright (−83 to −73 dBm), black (−73 to −63 dBm), dim (−63 to −53 dBm), bright (−53 to −43 dBm), black (−43 to −33 dBm). Range marks are every 20 km.

2. Description of radars and radar data acquisition and processing

NSSL's Norman Doppler radar is located at Max Westheimer airfield in Norman, Okla., and the remote Doppler radar at Cimarron airfield in Oklahoma City, 41.39 km and 309.9° from Norman (Fig. 2). These radars are closely matched, with specific characteristics listed in Table 1. Both are equipped with digital

TABLE 1. Characteristics of the Doppler radars.

	Norman	Cimarron
Wavelength (cm)	10.52	10.94
Peak power (KW)	750	500
Pulse length [μs (m)]	1 (150)	1 (150)
Half-power beam width (deg)	0.81°	0.85°
Nyquist velocity co-interval (m s^{-1})	±34.2	±35.6
PRT (μs)	768	768
Antenna gain including waveguide and radome transmission loss (dB)	44.8	43.2

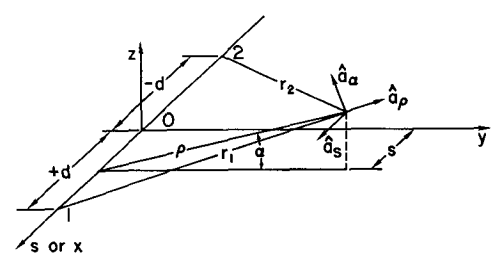

FIG. 4. Cylindrical coordinate system used for dual-Doppler analysis. The radars are located at the points 1 and 2, and a_ρ, a_s, a_α are the unit normals defining direction for the three velocity components.

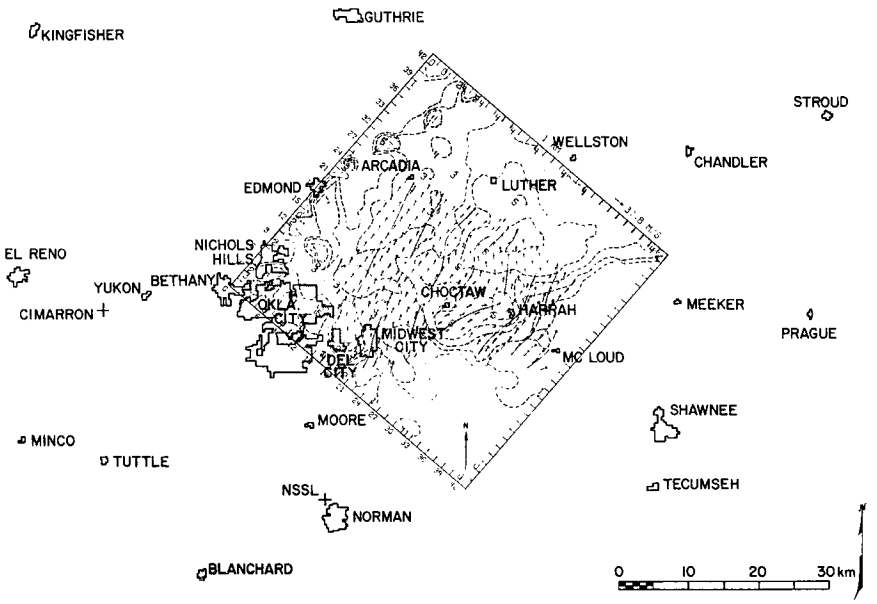

FIG. 5. Map of central Oklahoma with reflectivity field and winds relative to the ground at height of 1 km superimposed. Velocity scale vector is shown along eastern corner of box. This velocity is the maximum at this height. Reflectivity contours are labeled as log$Z$.

integrators that provide 512 range samples spaced 210 m apart, each with exponentially time-weighted (time constant=48.8 ms) signal power averages which are recorded for later construction of reflectivity fields. Digital integrator output is also quantized in about 10 dB steps for display on a PPI (Fig. 3) to assist data acquisition.

Doppler data are derived from complex (in-phase I and quadrature-phase Q) video echoes, digitally recorded in blocks of 64 time samples for each group of 16 equally spaced (300 m) range gates that are advanced in range as a group after each time block is recorded. In this way Doppler samples spanning the storm are successively accumulated as the antennas scan at 2° s^{-1}. Each block of 64 samples is processed, in post analysis, to estimate a Doppler spectrum mean

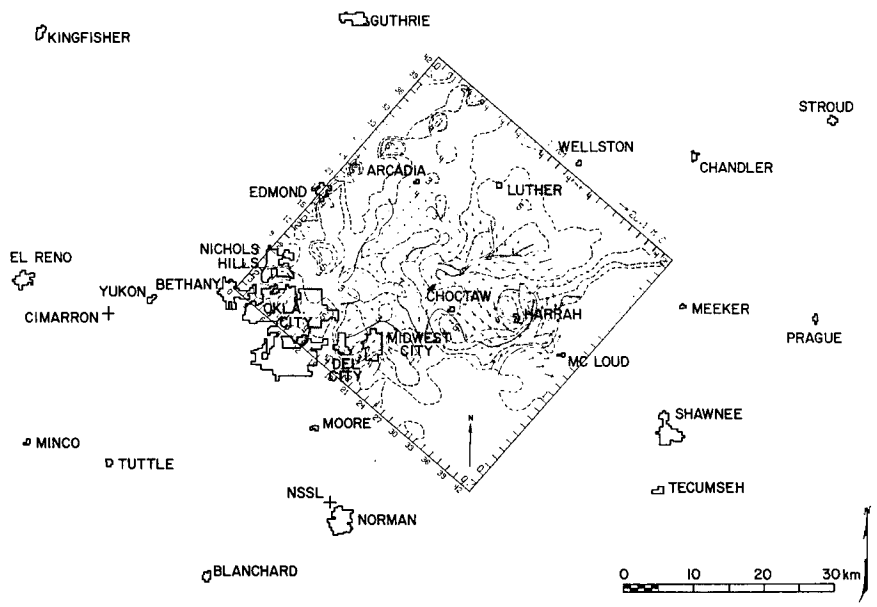

FIG. 6. Map of central Oklahoma with reflectivity field and winds relative to the mean at 1 km. Reflectivity contours are labeled as log$Z$.

velocity and width from computed covariance at the PRT (pulse repetition time) interval (Miller and Rochwarger, 1972; Sirmans and Bumgarner, 1975).

The area of common Doppler coverage for low elevation angles is illustrated by the sector (Fig. 2) within the square area outlining the array used in this analysis. Grid-point spacing is indicated by the dots in the lower right-hand corner. The array extends beyond the Doppler data area to display reflectivity fields over the larger data field provided by the digital integrators. Data collection was coordinated so that data within each quasi-horizontal sector were taken at nearly the same time, with elevation steps of about 1°. Azimuthal spacings were 2° (Norman) and 1° (Cimarron), range gate spacings were 300 m for both, and the maximum elevation attained was 16° at Norman and 8° at Cimarron. The stippled arrow through the sector (Fig. 2) encompasses points of intermittent tornado damage and is an estimate of the tornado's path based on this damage.

Fig. 3 is a PPI display of received power (Norman radar at 0.3° elevation). Range marks circles are spaced every 20 km. An interesting feature that prompted collection was the weak echo intrusion into a region of high reflectivity at about 40 km range and 40° azimuth, suggesting a region of inflow and probable cyclone

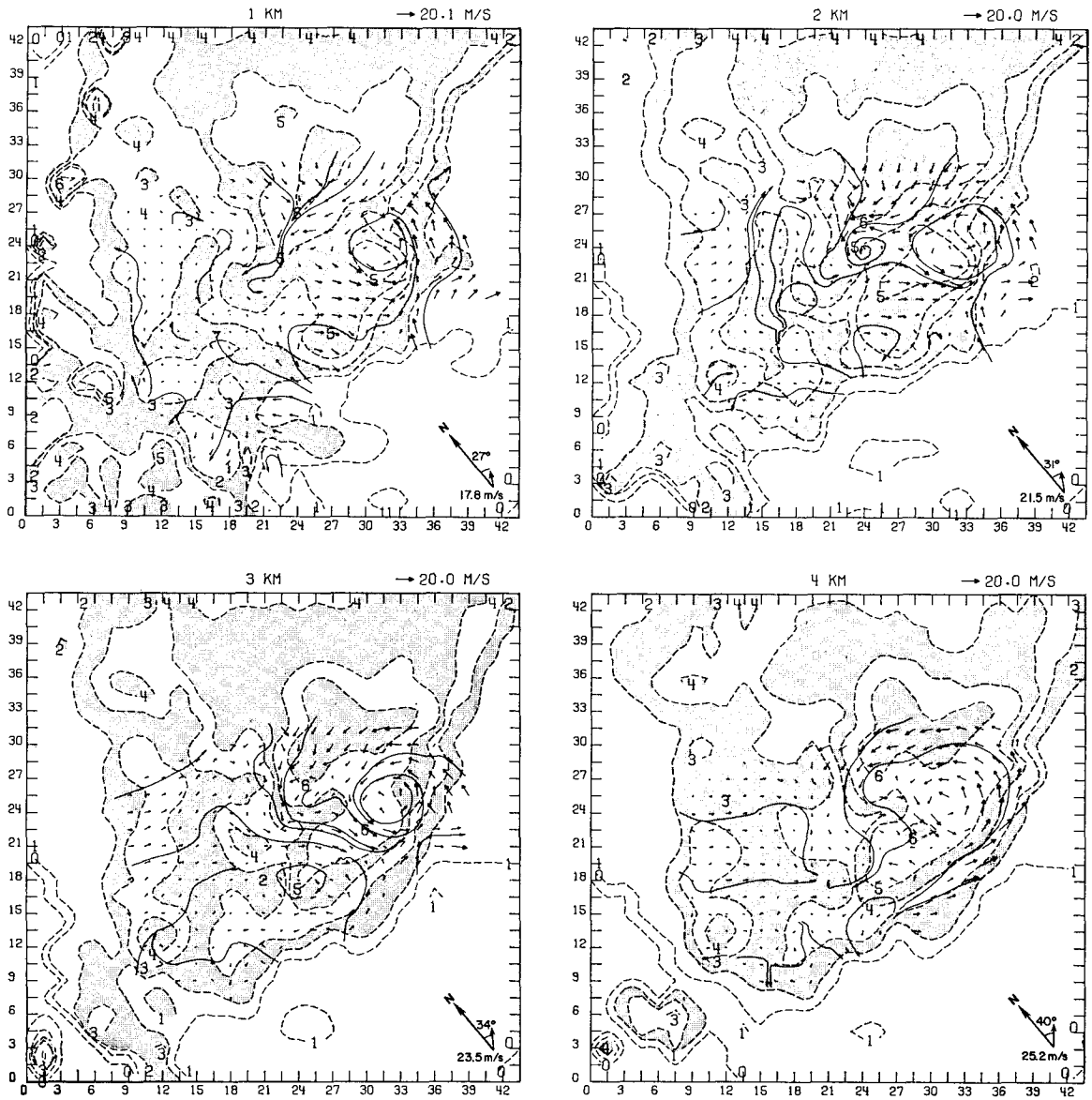

FIG. 7. Reflectivity field and the deviation from the mean horizontal velocity at four heights. Scales are in kilometers with origins at $x=-10$, $y=+15$ (Fig. 4). Arrow next to the north vector indicates mean wind at that level. Reflectivity contours are labeled as log$Z$.

circulation. Furthermore, there are reflectivity gradients of nearly 100 dB km^{-1} in places along the storm's southern edge. At this elevation angle, ground clutter and second trip due to range aliasing are evident out to 25 km (20°–30°) in Fig. 3. Second-trip echoes come from a storm that is beyond the unambiguous range interval (115 km). The region of maximum received power at 40 km range and 30° corresponds to a reflectivity in excess of 50 dBZ (see Fig. 5).

3. Analysis

It is desirable to solve for Cartesian components of the synthesized wind field and although these components can be derived directly from the Doppler velocities and continuity equation, this derivation necessitates a solution of an inhomogeneous hyperbolic partial differential equation to determine vertical wind (Armijo, 1969). Analysis is simplified in a cylindrical coordinate system where Cartesian wind components are derived from synthesized cylindrical wind components. The coordinate system is shown in Fig. 4 where radars (1, 2) are located at $+d$, $-d$, respectively. The analysis consists of (i) spatial interpolation of Doppler velocities to grid points located on ρ, s surfaces (α=constant); (ii) synthesis of Doppler velocities to derive the orthognal cylindrical wind components W_ρ, W_s; (iii) integration of the mass continuity equation to determine W_α;

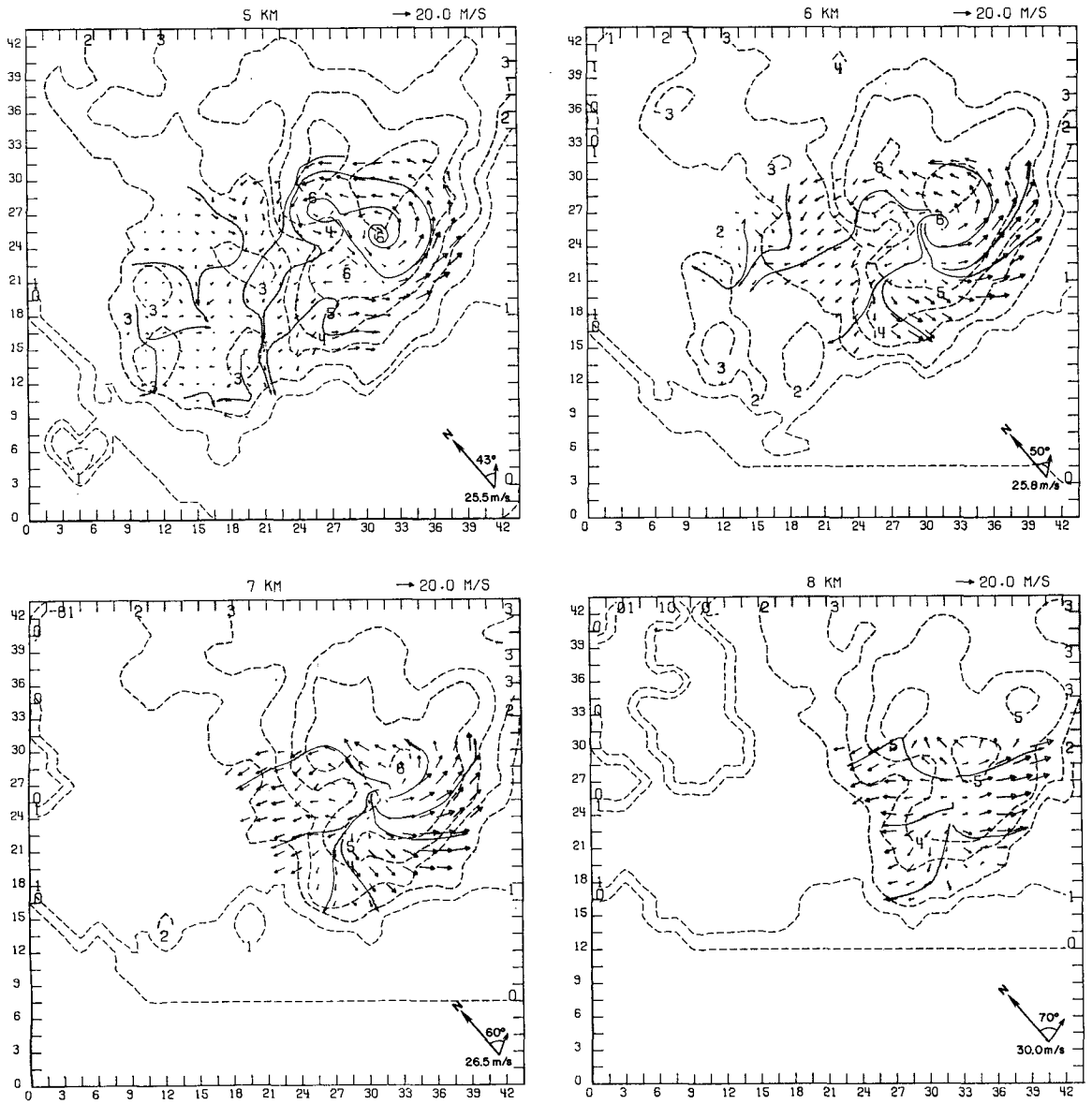

FIG. 8. As in Fig. 7 except that the origin has been adjusted to (−10.0, 15.0).

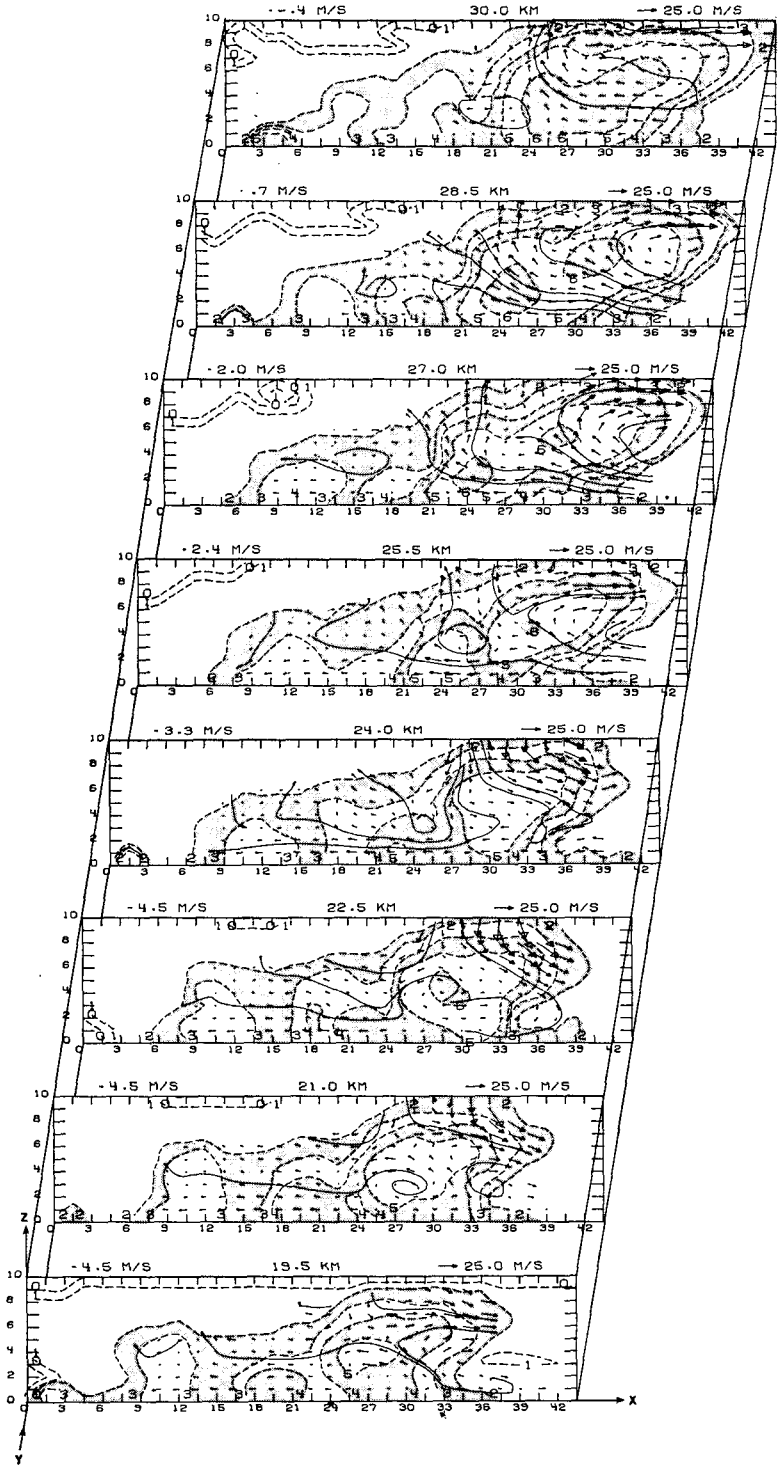

FIG. 9. Reflectivity and velocity fields in the x, z plane for eight planes. The mean horizontal velocity in each vertical plane was removed and is indicated in the upper left of each plane. Reflectivity contours are labeled as log$Z$.

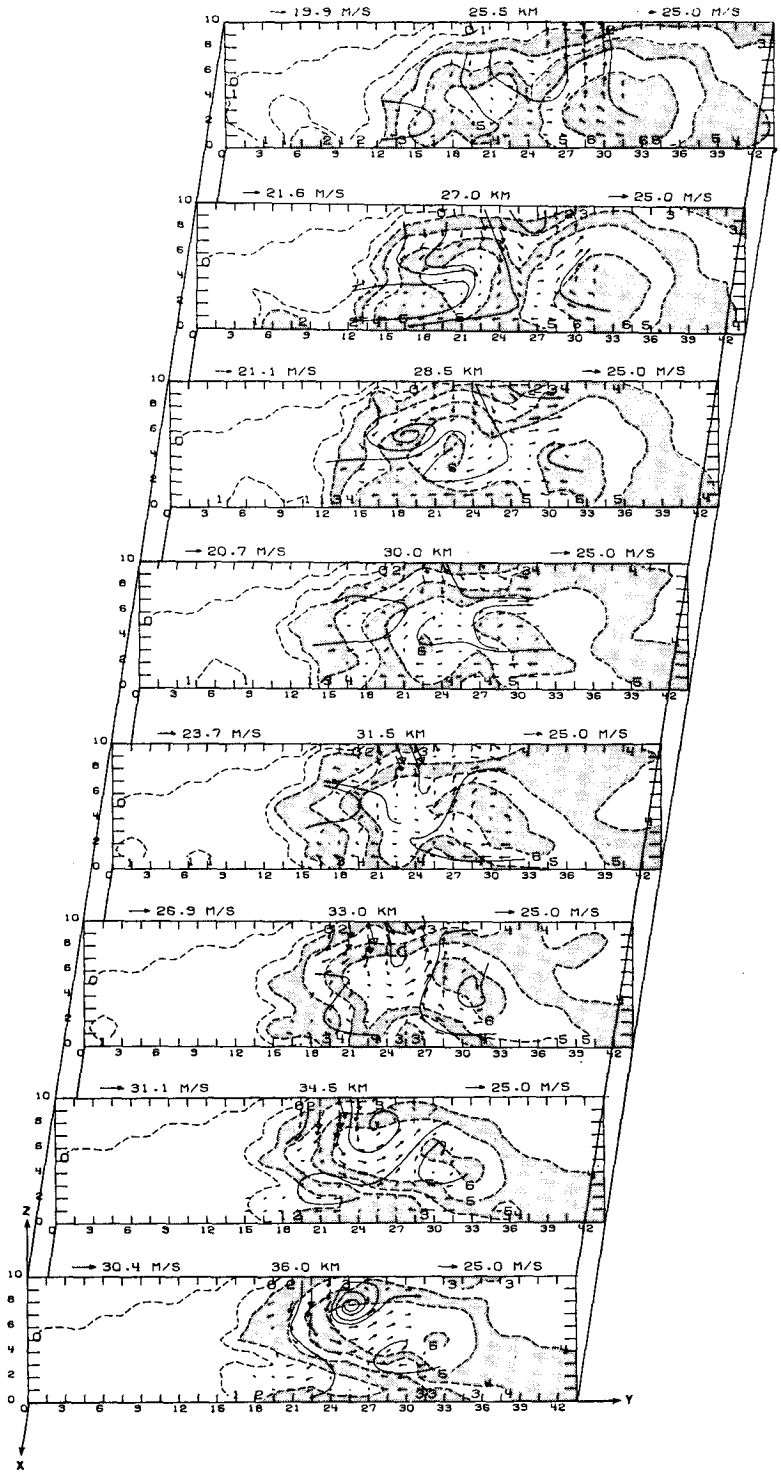

FIG. 10. As in Fig. 9 except for the y,z plane.

and (iv) interpolation to Cartesian coordinates. Reflectivity fields are determined by distance-weighting the power measured by each radar. Further analysis details may be found in the Appendix.

4. Observations

Fig. 5 shows the synthesized reflectivity and wind fields at a height of 1 km. The origin has been adjusted to $x=-10$, $y=15$ km. Comparison of log reflectivity contours (Fig. 5) and the PPI display (Fig. 3) can only be made in a qualitative way because the latter is a display of average received power (i.e., range normalization is not present), and reflectivity contours, derived from smoothed data, do not exhibit the smaller scales evident in Fig. 3. In both Figs. 3 and 5 the weak echo region is apparent at about 40 km from Norman at 40°. The second bright intensity category in Fig. 3 from 35 to 55 km corresponds to about $\log Z \geqslant 5$ beyond 40 km and $\log Z \geqslant 4$ closer to the radar. Receiver saturation occurred for received power greater than -40 dBm and thus reflectivities greater than $Z=10^{5.5}$ (at $R \approx 40$ km) are underestimated.

The horizontal wind field relative to the ground is shown in Fig. 5. Streamlines have been drawn in addition to velocity vectors, whose length is proportional to wind speed. From the curvature in the streamlines it is evident that appreciable local vorticity exists in the region near the grid point 30.0, 24.0.

To view the kinematics at 1 km relative to the mean wind $\bar{V}$, the deviation $V'=V-\bar{V}$ was computed. The relative velocity field thus derived from the data displayed in Fig. 5 is shown in Fig. 6. Cyclonic circulations are also apparent. These are associated with regions of maximum updrafts as will be shown later. The velocity fields are in general agreement with present storm models, particularly in the weak echo region where both imply a strong updraft.

Reflectivities and velocities relative to the mean at heights from 1 to 8 km at 1 km intervals are shown in Figs. 7 and 8. Cyclonic rotation is evident in the region centered at coordinates 30.0, 24.0 at least through 7 km. The level of non-divergence appears to be about 5 km. A second vorticity center exists about 24.0, 24.0. These two circulations, manifested in curved streamlines, are evident in Fig. 5 at range 39 km and azimuths 40° and 32°, respectively. The plane nearest to the inflow (labeled 27.0 km in Fig. 9) shows ascending air in the region of the two circulations. The major circulation centered at 30.0, 24.0 is bisected by the fourth plane from the bottom in Fig. 9 and the fifth from the bottom in Fig. 10. A strong downdraft is found to the SW of the circulation whereas the updraft is concentrated in the weak echo region to the NE. Large reflectivities ($Z \geqslant 10^6$) and ascending air are correlated at mid-levels. The high reflectivities shown in these figures imply the existence of hail (Barge, 1974); indeed, much was reported. The coincidence of high reflectivities and updrafts provides support for the generation and concentration of these hydrometeors.

The mean horizontal wind in the analyzed portion of the storm (see Figs. 7 and 8) does not differ much from environmental wind at the same level (see Fig. 1). This suggests that, at least for a large portion of the storm, measured wind velocities are a combination of the internal and environmental flow.

5. Summary

This analysis of wind and reflectivity fields associated with a tornadic storm reveals two strong vorticity centers, which are a maximum at 5 km, the apparent level of non-divergence. Many smaller eddies relative to the mean wind are also present. Strong updrafts are within the two largest circulations. One of these is clearly associated with the weak echo region and is NE of the strongest circulation, which is centered over the inferred tornado path. To the SW of this circulation is a strong downdraft. Updrafts important in the growth and concentration of hail, which this storm produced in quantity, are also correlated with regions of high reflectivity ($Z > 10^6$).

Acknowledgments. The authors acknowledge Dr. G. L. Achtemeier of Illinois State Water Survey for his contribution in developing the contour and streamline plotting subroutines.

The authors express their appreciation to the members of the NSSL staff who have rendered support to the dual-Doppler project. Recognition is made to Messrs. R. Brown and D. Burgess who coordinated the dual-Doppler data acquisition and to Messrs. Anderson and Shinn for their operation of the radars and data collection processing equipment. Recognition is made to Dr. Philippe Waldteufel of Centre National d'Études des Télécommunications and to Dr. D. Zrnic of California State University at Northridge. These experiments were made possible in part through the support of the FAA under Interagency Agreement DOT-FA72-WAI-265 and the AEC under Interagency Agreement AT(49-5)1289.

Acknowledgement is also made to Mrs. Jennifer Farris for her efforts in preparing the figures, and to Ms. Dorothea Gadberry, Judy Turner and Deborah Killian for typing the manuscript.

APPENDIX

Objective Analysis

Prior to interpolation, data locations are adjusted to accommodate storm translation. For this purpose the storm structure is assumed stationary over the collection period (4 min) and observations are translated by an amount proportional to the time difference between data collection time and a reference time midway within the acquisition period. Storm motion was esti-

mated by visually correlating successive PPI scans at 0.3° elevation. Storm advection was thus estimated to be 15 m s^{-1} from 220°. Since the change in angular position of any data point during data collection was less than 3.0°, the change in Doppler velocity due to storm displacement was assumed negligible. Earth curvature causes local zeniths between radars to differ by nearly 0.4° which is appreciable with respect to antenna beam width. To correct for this, azimuthally dependent adjustments to data elevation angles were made to effectively put radars on a flat earth with parallel vertical axes. In all computations, a $\frac{4}{3}$ earth radius model has been assumed.

Interpolation is a distance-weighted average of all data contained within an oblate spheroidal volume having a horizontal semi-axis R_H(1.5 km) and a vertical semi-axis R_Z(1.0 km). A Cressman filter (Cressman, 1959)

$$W_i=\frac{R_i^2-D_i^2}{R_i^2+D_i^2} \tag{A1}$$

was chosen to determine the weight W_i applied to each datum located a distance D_i from the grid point, where the influence radius R_i is

$$R_i=\frac{R_H R_Z}{(R_H^2\sin^2\psi_i+R_Z^2\cos^2\psi_i)^{\frac{1}{2}}}, \tag{A2}$$

$$\psi_i=\tan^{-1}\left[\frac{z_i}{(x_i^2+y_i^2)^{\frac{1}{2}}}\right], \tag{A3}$$

and x_i, y_i, z_i are the data coordinates relative to the grid point.

Thus, interpolated mean Doppler velocities $\bar{V}_1$ (or $\bar{V}_2$) and reflectivity $\bar{Z}$ are given by

$$\bar{V}_{1(2)};\bar{Z}=\sum_{i=1}^{N} W_i(V_{i,1(2)};Z_i)/\sum_{i=1}^{N} W_i, \tag{A4}$$

where N is the total number of data within the averaging volume.

The cylindrical wind components in the ρ, s plane (Fig. 4) are related to $\bar{V}_1$, $\bar{V}_2$, as

$$\left.\begin{aligned} W_\rho&=\frac{(s+d)r_1\bar{V}_1-(s-d)r_2\bar{V}_2}{2d\rho}-\bar{V}_t\sin\alpha \\ W_s&=\frac{r_2\bar{V}_2-r_1\bar{V}_1}{2d}\end{aligned}\right\}, \tag{A5}$$

where $\bar{V}_t$ is the hydrometeor terminal velocity. Assuming liquid water, terminal velocity is estimated from the interpolated reflectivity (Joss and Waldvogel, 1970):

$$\bar{V}_t=2.6\bar{Z}^{0.107}\left(\frac{\gamma_0}{\gamma}\right)^{0.4}, \tag{A6}$$

where the parenthetical term is a correction suggested by Foote and du Toit (1969) to account for height-dependent air density γ. No attempt in this preliminary analysis is made to differentiate regions of liquid and solid precipitation for which different $\bar{V}_t$, $\bar{Z}$ relations would be required.

To avoid artificially extending the boundaries by extrapolation or using an interpolated estimate with too great a variance, no value was assigned to those grid points for which the sum of weights was less than 2.0. If a grid location had no assigned value but was surrounded on at least three sides by interpolated ones, then a second distance-weighted interpolation was applied to obtain a grid value from the adjacent grid points. The weights were inversely proportional to distance in the ρ, s plane and a weight of 0.5 was given to grid values directly above or below.

The alpha component W_α of wind, quasi-vertical for small α, is obtained by solving the continuity equation in cylindrical coordinates:

$$\frac{1}{\rho}\frac{\partial}{\partial\rho}(\rho\gamma W_\rho)+\frac{1}{\rho}\frac{\partial}{\partial\alpha}(\gamma W_\alpha)+\frac{\partial}{\partial s}(\gamma W_s)=0, \tag{A7}$$

where the mass density γ is given by

$$\gamma=\gamma_0\exp[-gM\rho\sin\alpha/(RT)], \tag{A8}$$

and g is the gravitational constant (9.8 m s^{-2}), M the mean molecular weight of air (29 g mol^{-1}), T the absolute temperature (estimated to be 296 K at the surface), and R the universal gas constant (287.04 m^2 s^{-2} K^{-1}). A lapse rate of 5.75 K km^{-1} is assumed. Integrating (A7) between $\alpha_{i-\frac{1}{2}}$ and $\alpha_{i+\frac{1}{2}}$ yields

$$W_\alpha(\rho,\alpha_i,s)=\frac{\gamma_{i-\frac{1}{2}}}{\gamma_i}W_\alpha(\rho,\alpha_{i-\frac{1}{2}},s) -\frac{1}{2}\int_{\alpha_{i-\frac{1}{2}}}^{\alpha_{i+\frac{1}{2}}}\left[\rho\left(\frac{\partial^W\rho}{\partial\rho}+\frac{\partial^W s}{\partial s}\right)+W_\rho\left(1+\frac{\rho}{\gamma}\frac{\partial\gamma}{\partial\rho}\right)\right]d\alpha, \tag{A9}$$

where $\alpha_i=(i-1)\Delta\alpha$, and γ_i is assumed to be constant over the interval $\Delta\alpha$. The plane $\alpha=0$ is parallel to the tangent plane at station midpath but does not coincide with the earth's surface; thus, W_α $(\rho,0,s)$ may not be zero. Therefore to obtain a boundary condition at grid-point (ρ,α,s), W_α is assumed equal to zero when $\alpha=\alpha'$, the depression angle required to have the grid point on the earth. That is,

$$W_\alpha(\rho,\alpha',s)=0 \tag{A10}$$

at

$$\alpha'\approx-\frac{\rho}{2a_e}\equiv\alpha_{\frac{1}{2}}, \tag{A11}$$

where a_e is the effective earth's radius.

To reduce the variance of the analyzed fields prior to integration, W_ρ and W_s fields were smoothed by the subjectively chosen two-dimensional Shuman filter

(Shuman, 1957) given by

$$W_{\rho(s)}=\tfrac{1}{4}W_{0,\rho(s)}+\tfrac{1}{8}\sum W_{1,\rho(s)}+\tfrac{1}{16}\sum W_{2,\rho(s)}. \quad \text{(A12)}$$

Here ΣW_1 and ΣW_2 are the sums of the values at distances 1 and $\sqrt{2}$ grid lengths from the point with value $W_{0,\rho(s)}$ being adjusted to $W_{\rho(s)}$.

The Cartesian components u, v, w of the wind, in the x, y, z directions, respectively, are then determined and interpolated to grids consisting of a series of constant altitude planes spaced 1 km apart with a horizontal grid spacing of 1.5 km. The interpolation procedure was identical to that used to transform original data to constant α planes except now $R_H=R_Z=1.0$ km. The Cartesian components are then used to determine the wind vector in horizontal and vertical planes.

REFERENCES

Armijo, L., 1969: A theory for the determination of wind and precipitation velocities with Doppler radars. *J. Atmos. Sci.*, **26**, 570–573.

Barge, B. L., 1974: Polarization measurements of precipitation back-scatter in Alberta. *J. Rech. Atmos.*, **8**, 163–173.

Cressman, G. P., 1959: An operational objective analysis system. *Mon. Wea. Rev.*, **87**, 367–374.

Foote, G. B., and P. S. du Toit, 1969: Terminal velocity of raindrops aloft. *J. Appl. Meteor.*, **8**, 249–253.

Frisch, A. S., L. J. Miller and R. G. Strauch, 1974: Three-dimensional air motion measured in snow. *Geophy. Res. Lett.*, **1**, 86–89.

Joss, J., and A. Waldvogel, 1970: Raindrop size distribution and Doppler velocities. *Preprints 14th Radar Meteorology Conference*, Tucson, Ariz., Amer. Meteor. Soc., 153–156.

Lhermitte, R., 1970: Dual-Doppler radar observations of convective storm circulation. *Preprints 14th Radar Meteorology Conference*, Tucson, Ariz., Amer. Meteor. Soc., 139–144.

Miller, K. S., and M. M. Rochwarger, 1972: A covariance approach to spectral moment estimation. *IEEE Trans. Information Theory*, **IT-18**, 588–596.

Shuman, F. G., 1957: Numerical methods and weather predictions II. Smoothing and filtering. *Mon. Wea. Rev.*, **85**, 357–361.

Sirmans, D., and B. Bumgarner, 1975: Numerical comparison of five mean frequency estimators. *J. Appl. Meteor.*, **14**, 991–1003.